The effects of stoichiometry on the mechanical properties of icosahedral boron carbide under loading

2012 J. Phys.: Condens. Matter 24 505402

(http://iopscience.iop.org/0953-8984/24/50/505402)

Report Documentation Page

Form Approved
OMB No. 0704-0188

1. REPORT DATE	2. REPORT TYPE	3. DATES COVERED
19 NOV 2012		**00-00-2012 to 00-00-2012**

4. TITLE AND SUBTITLE	5a. CONTRACT NUMBER
The effects of stoichiometry on the mechanical properties of icosahedral boron carbide under loading	5b. GRANT NUMBER
	5c. PROGRAM ELEMENT NUMBER
6. AUTHOR(S)	5d. PROJECT NUMBER
	5e. TASK NUMBER
	5f. WORK UNIT NUMBER
7. PERFORMING ORGANIZATION NAME(S) AND ADDRESS(ES) **US Army Research Laboratory,Aberdeen Proving Ground,MD,21005**	8. PERFORMING ORGANIZATION REPORT NUMBER
9. SPONSORING/MONITORING AGENCY NAME(S) AND ADDRESS(ES)	10. SPONSOR/MONITOR'S ACRONYM(S)
	11. SPONSOR/MONITOR'S REPORT NUMBER(S)

12. DISTRIBUTION/AVAILABILITY STATEMENT
Approved for public release; distribution unlimited

13. SUPPLEMENTARY NOTES

14. ABSTRACT
The effects of stoichiometry on the atomic structure and the related mechanical properties of boron carbide (B4C) have been studied using density functional theory and quantum molecular dynamics simulations. Computational cells of boron carbide containing up to 960 atoms and spanning compositions ranging from 6.7% to 26.7% carbon were used to determine the effects of stoichiometry on the atomic structure, elastic properties, and stress?strain response as a function of hydrostatic, uniaxial, and shear loading paths. It was found that different stoichiometries, as well as variable atomic arrangements within a fixed stoichiometry can have a significant impact on the yield stress of boron carbide when compressed uniaxially (by as much as 70% in some cases); the significantly reduced strength of boron carbide under shear loading is also demonstrated.

15. SUBJECT TERMS

16. SECURITY CLASSIFICATION OF:			17. LIMITATION OF ABSTRACT	18. NUMBER OF PAGES	19a. NAME OF RESPONSIBLE PERSON
a. REPORT **unclassified**	b. ABSTRACT **unclassified**	c. THIS PAGE **unclassified**	**Same as Report (SAR)**	**12**	

J. Phys.: Condens. Matter **24** (2012) 505402 (11pp) doi:10.1088/0953-8984/24/50/505402

The effects of stoichiometry on the mechanical properties of icosahedral boron carbide under loading

DeCarlos E Taylor[1,3], James W McCauley[1] and T W Wright[2]

[1] US Army Research Laboratory, Aberdeen Proving Ground, MD 21005, USA
[2] Department of Mechanical Engineering, Johns Hopkins University, Baltimore, MD 21218, USA

E-mail: decarlos.e.taylor.civ@mail.mil and james.w.mccauley.civ@mail.mil

Received 13 July 2012, in final form 15 October 2012
Published 19 November 2012
Online at stacks.iop.org/JPhysCM/24/505402

Abstract
The effects of stoichiometry on the atomic structure and the related mechanical properties of boron carbide (B_4C) have been studied using density functional theory and quantum molecular dynamics simulations. Computational cells of boron carbide containing up to 960 atoms and spanning compositions ranging from 6.7% to 26.7% carbon were used to determine the effects of stoichiometry on the atomic structure, elastic properties, and stress–strain response as a function of hydrostatic, uniaxial, and shear loading paths. It was found that different stoichiometries, as well as variable atomic arrangements within a fixed stoichiometry, can have a significant impact on the yield stress of boron carbide when compressed uniaxially (by as much as 70% in some cases); the significantly reduced strength of boron carbide under shear loading is also demonstrated.

(Some figures may appear in colour only in the online journal)

1. Introduction

Boron carbide (BC), due to its extreme hardness, low density, and demonstrated performance, has been used as an armor ceramic for many years [1]. With nominal stoichiometry B_4C, the crystal structure consists of 12-atom icosahedra cross-linked by 3-atom chains as shown in figure 1. Within the structure, there is a high degree of compositional variation with configurations consisting of B_{12} or $B_{11}C$ icosahedra (among others) linked by a variety of 3-atom chains such as C–C–C and C–B–C. BC is generally regarded to have $R\bar{3}m$ symmetry [2], however this can only be true for a *subset* of the available atomic arrangements since placement of even a single carbon atom within an icosahedron causes a monoclinic distortion of the rhombohedral lattice thereby reducing the crystalline symmetry [3]. Configurations of different stoichiometry from ideal B_4C (e.g. $B_{2.75}C$ or $B_{5.6}C$) are referred to as 'polytypoids' and atomic configurations with ideal B_4C stoichiometry, but different arrangement of atoms within the icosahedra (or chains), are termed 'polytypes'. Within each icosahedron, there exist two crystallographically unique sites termed 'polar' and 'equatorial' as shown in figure 2 and hereafter, any atom that specifically occupies a polar or equatorial site within an icosahedron will be labeled with a subscript 'p' or 'e' respectively.

Experimentally, BC can be produced by several methods such as reaction of boric oxide and carbon in an electric arc furnace [4] or carbothermal reduction of a boric acid–citric acid gel [5]. The powders can consist of a range of boron to carbon ratios resulting in a complex phase diagram [6], an example of which is shown in figure 3. Other phase diagrams have also been constructed [7–9]. A new phase equilibrium diagram has just recently been submitted for publication [10] which suggests that stoichiometric B_4C is a line compound with a monoclinic structure that is stable to 600 K. In addition, it is also suggested that a rhombohedral $B_{13}C_2$ solid solution phase is the stable phase above 600 K from about 10 to 20 atomic %C. The issue of a $B_{13}C_2$ phase has been debated for some time after first being identified by Samsonov *et al* in 1956 [11]. In a recent review article [8]

[3] Author to whom any correspondence should be addressed.

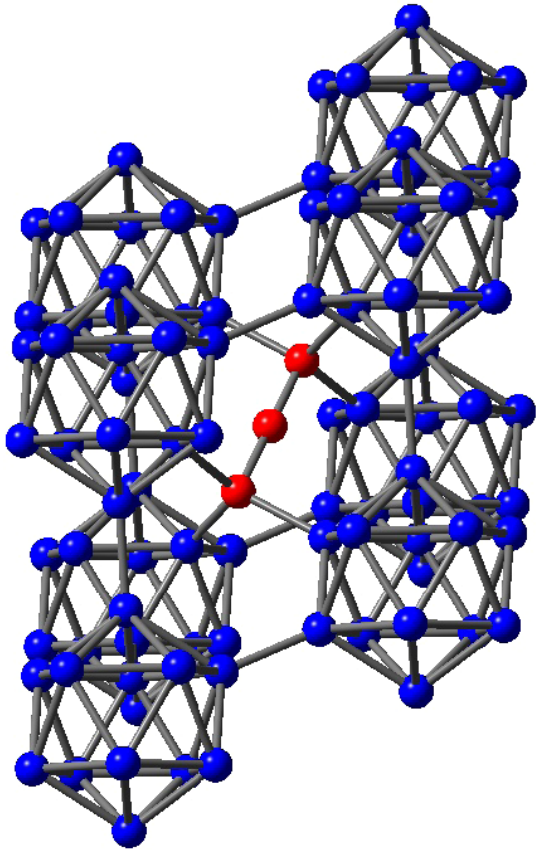

Figure 1. Icosahedral structure of boron (blue) carbide linked by a 3-atom carbon (red) chain. For clarity of representation, only a single chain is included in the image.

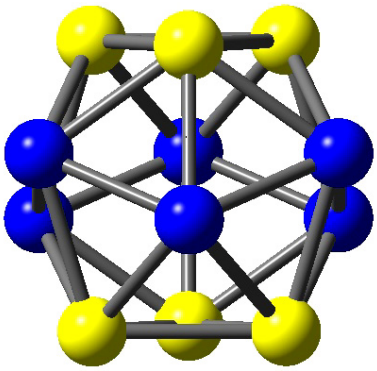

Figure 2. Icosahedron with polar (yellow) and equatorial (blue) positions.

it has been suggested that x-ray diffraction analysis of a series of boron-rich materials indicates a distinct change in the *c* lattice parameters at about 13 atomic %C, the $B_{13}C_2$ composition. Further, in that work, a single crystal of BC was chemically analyzed by Raman spectroscopy and it is clear that even 'single crystals' of BC can have significant stoichiometric variation. McCuistion *et al* [12] compiled chemical compositions of a variety of BC powders also indicating B/C ratios from 3.58 to 4.0. The exact chemical composition of BC grains in two commercial bulk materials was determined by Chen *et al* [13] using Electron Energy Loss Spectroscopy (EELS) with the following results: B/C ratios of

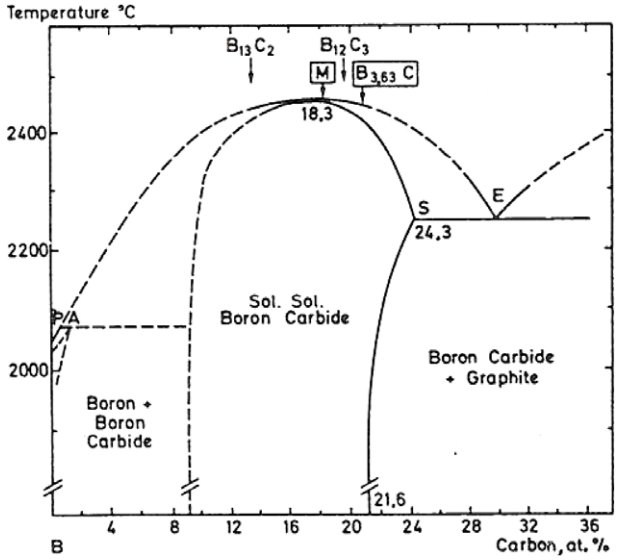

Figure 3. Boron carbide phase diagram. Reproduced with permission from [6]. Copyright 1983 Elsevier.

Table 1. Experimental bulk and shear moduli (GPa) of boron carbide as a function of composition.

Stoichiometry	% Carbon	Bulk modulus	Shear modulus
B_4C	20.0	235	197
$B_{4.5}C$	18.2	237	197
$B_{5.6}C$	15.2	236	197
$B_{6.5}C$	13.3	231	189
$B_{7.7}C$	11.5	178	150

3.81 ± 0.15 and 3.90 ± 0.07. These variations in composition have an effect on the observed mechanical properties, as shown in table 1, where the experimentally measured bulk and shear moduli for samples ranging from B_4C (20% carbon) to $B_{7.7}C$ (11.5% carbon) are presented [8]. The general trend evidenced by the experimental data is a reduction in stiffness as the boron concentration increases. There has been much work on determination of the structure and properties of BC samples of varying composition. Conde *et al* [14] determined the hexagonal lattice parameters of B_4C samples ranging from 10% to 20% C using glancing incidence x-ray diffraction and similar experimental studies of structure as a function of stoichiometry were conducted by Konovalikhin and Ponomarev [15] and Kwei and Morosin [16]. The application of solid state density functional theory (DFT) [17] by Saal *et al* [18] and Vast *et al* [19] provided theoretically determined structures and energies for a range of stoichiometries.

Although the structure and formation enthalpy of BC as a function of stoichiometry has been well documented [18], knowledge of the origins of the deformation and damage mechanisms, and their relation to the macro-mechanical properties, is critical. The discovery of shock-induced localized nanoscale amorphization [20] in hot pressed bulk BC and its relationship to performance is unclear. In addition, the origin of the dramatic loss in shear strength [21, 22] of B_4C in plate impact experiments has not been elucidated. The elastic moduli of 3 BC polytypes, all with 20%

carbon composition, were predicted using DFT by Taylor *et al* [23] and Aryal *et al* [24] under hydrostatic and uniaxial load. Taylor *et al* showed that among the B_{12}(C–C–C), $B_{11}C_p$(C–B–C), and $B_{11}C_e$(C–B–C) polytypes, there was a reduction in the bulk modulus from 234 to 222 GPa when going from a C–B–C to a C–C–C chain at fixed 20% C composition and polytypism was shown to affect the pressure evolution of the elastic moduli as well. Aryal *et al* [24] presented similar results for the elastic moduli under uniaxial load and also presented stress–strain curves for two BC polytypes, both containing 20% carbon and showed that there was a slight difference in the stress–strain response between the two polytypes studied in that work.

Since BC powders are most likely a mixture of BC stoichiometries [8], and given the experimentally observed effect of such compositional variation on the mechanical response of BC, it is important that the mechanical properties of a diversity of compositions be well characterized. This information can play a role in identification of 'soft' configurations that may initiate failure in the BC structure when impacted with high velocity projectiles. In this paper, we present a comprehensive survey, using DFT, of the mechanical properties of 15 BC structures with stoichiometries ranging from $B_{2.75}C$ to $B_{14}C$ as shown in table 2. The $B_{2.75}C$ stoichiometry (26% C) represents a carbon-rich example and, as indicated by the phase diagram in figure 3, would precipitate carbon in the form of graphite at high processing temperatures. However, it was included in the current analysis purely as an example of an extremely carbon rich limit in order to further elucidate the effects of stoichiometry on the mechanical properties of the icosahedral structures under consideration. For each stable configuration, the structure, elastic moduli, and stress–strain response under several loading paths using quantum molecular dynamics (MD) simulations have been determined. We include an analysis of the stress–strain response of each structure under shear, in addition to hydrostatic and uniaxial loading, since shear has been postulated to be a contributing factor to the pressure-induced amorphization [25] phenomenon that has been observed experimentally in BC. The computational approach adopted in this work is described in section 2, followed by presentation of the results and discussion in sections 3 and 4 respectively.

2. Computational approach

2.1. Crystal structure optimization algorithm

A crystal structure optimization program was written, based on the L-BFGS [26] optimization algorithm, where any stress state (hydrostatic, uniaxial, shear) can be imposed. Several software packages (such as CP2K [27]) already offer such implementations, however, many of those programs rotate the input coordinates to a different computational orientation making interpretation of the stress along a specific crystallographic direction, a key component of this work, more difficult to monitor and interpret. To circumvent this difficulty, a program that does not perform a rotation of the input orientation was written and used in this study. At each optimization step, the energy, forces, and stress tensor were evaluated using the Perdew–Burke–Ernzerhof [28] (PBE) functional in a double zeta valence plus polarization basis set with a plane wave cutoff of 800 Ryd provided by the CP2K [27] program. It should be noted that no symmetry restrictions were imposed, i.e., no constraints were applied to enforce linearity of the 3-atom chain. For each system, a $2 \times 2 \times 2$ computational supercell containing 120 atoms was used in order to minimize size effects introduced when using smaller computational cells. At each optimization step, the stress tensor returned by CP2K was converted to cell vector derivatives, required by the L-BFGS algorithm to update the lattice vectors, using the transformation from stress to cell vector gradients given by Doll [29]. Optimization was considered converged when the gradient norm of the cell vector derivatives was below 0.0001 atomic units.

Table 2. Boron carbide stoichiometries used in this study. The subscript e and p labels denote equatorial and polar carbons, respectively.

Structure	Stoichiometry	% C
$B_{11}C_e$(CCC)	$B_{2.75}C$	26.66
$B_{11}C_p$(CCC)	$B_{2.75}C$	26.66
B_{12}(CCC)	B_4C	20.00
$B_{11}C_e$(CCB)	B_4C	20.00
$B_{11}C_p$(CCB)	B_4C	20.00
$B_{11}C_e$(CBC)	B_4C	20.00
$B_{11}C_p$(CBC)	B_4C	20.00
B_{12}(CCB)	$B_{6.5}C$	13.33
B_{12}(CBC)	$B_{6.5}C$	13.33
$B_{11}C_e$(BCB)	$B_{6.5}C$	13.33
$B_{11}C_p$(BCB)	$B_{6.5}C$	13.33
$B_{11}C_e$(BBC)	$B_{6.5}C$	13.33
$B_{11}C_p$(BBC)	$B_{6.5}C$	13.33
B_{12}(BBC)	$B_{14}C$	6.66
B_{12}(BCB)	$B_{14}C$	6.66

2.2. Elastic constants

Elastic constants are related to the second derivative of the total energy with respect to strain, ε_i, via

$$C_{ij} = \frac{1}{V}\frac{\partial^2 E}{\partial\varepsilon_i \partial\varepsilon_j}\bigg|_0 \tag{1}$$

where V is the unit cell volume and $i, j = 1 \cdots 6$ using the compact Voigt notation ($1 = xx, 2 = yy, 3 = zz, 4 = yz, 5 = xz, 6 = xy$). For this work, a program was written that evaluates the second derivatives in equation (1) via a finite difference of analytic first derivatives of the energy with respect to strain (stress tensor) provided by the CP2K code. We have monitored the change in the elastic constants as a function of hydrostatic and uniaxial load and the required stress corrections for elastic constants, C_{ijkl}, under non-zero load were included using:

$$B_{ijkl} = C_{ijkl} + \tfrac{1}{2}(\delta_{ik}\sigma_{jl} + \delta_{jk}\sigma_{il} + \delta_{il}\sigma_{jk} + \delta_{jl}\sigma_{ik} - 2\delta_{kl}\sigma_{ij}) \tag{2}$$

with σ_{ij} being an element of the stress tensor and B_{ijkl} representing the stress corrected effective elastic constant (or 'Birch coefficient') [30, 31].

Table 3. Computed unit cell parameters using 0 K geometry optimization and MD simulation (values in parentheses) at 298 K. The shaded gray area indicates that no stable configuration containing a *linear* 3-atom chain was found. (Lengths in Angstroms, angles in degrees, volume in cubic Angstroms).

Structure	Formula	% C	a	b	c	α	β	γ	Volume
Experiment[37]	$B_{5.6}C$	15.2	**5.19**	**5.19**	**5.19**	**65.18**	**65.18**	**65.18**	**110.02**
$B_{11}C_e$(CCC)	$B_{2.75}C$	26.66	**5.14(5.15)**	**5.21(5.22)**	**5.21(5.22)**	**64.31(64.28)**	**65.19(65.22)**	**65.19(65.22)**	**109.28(109.93)**
$B_{11}C_p$(CCC)	$B_{2.75}C$	26.66	**5.05(5.06)**	**5.21(5.22)**	**5.21(5.22)**	**64.86(64.82)**	**66.05(66.07)**	**66.05(66.07)**	**108.93(109.66)**
B_{12}(CCC)	B_4C	20.00	**5.19(5.21)**	**5.19(5.21)**	**5.19(5.21)**	**66.01(66.01)**	**66.01(66.01)**	**66.01(66.01)**	**112.09(112.81)**
$B_{11}C_e$(CCB)	B_4C	20.00	**5.16(5.17)**	**5.22(5.23)**	**5.22(5.23)**	**66.18(66.18)**	**66.16(66.16)**	**66.16(66.16)**	**112.72(113.38)**
$B_{11}C_p$(CCB)	B_4C	20.00	**5.05(5.06)**	**5.23(5.24)**	**5.23(5.24)**	**66.17(66.14)**	**67.33(67.35)**	**67.33(67.35)**	**112.27(112.90)**
$B_{11}C_e$(CBC)	B_4C	20.00	**5.18(5.18)**	**5.22(5.22)**	**5.22(5.22)**	**64.86(64.84)**	**64.97(64.97)**	**64.97(64.97)**	**110.16(110.77)**
$B_{11}C_p$(CBC)	B_4C	20.00	**5.07(5.08)**	**5.22(5.22)**	**5.22(5.22)**	**65.24(65.22)**	**66.07(66.08)**	**66.07(66.08)**	**109.75(110.43)**
B_{12}(CCB)	$B_{6.5}C$	13.33	**5.16(5.17)**	**5.22(5.22)**	**5.22(5.22)**	**66.79(66.81)**	**67.89(67.83)**	**67.89(67.83)**	**115.29(115.95)**
B_{12}(CBC)	$B_{6.5}C$	13.33	**5.20(5.21)**	**5.20(5.21)**	**5.20(5.21)**	**65.83(65.83)**	**65.83(65.83)**	**65.83(65.83)**	**112.10(112.76)**
$B_{11}C_e$(BCB)	$B_{6.5}C$	13.33							
$B_{11}C_p$(BCB)	$B_{6.5}C$	13.33							
$B_{11}C_e$(BBC)	$B_{6.5}C$	13.33							
$B_{11}C_p$(BBC)	$B_{6.5}C$	13.33							
B_{12}(BBC)	$B_{14}C$	6.66							
B_{12}(BCB)	$B_{14}C$	6.66							

2.3. Quantum molecular dynamics simulations

Quantum molecular dynamics simulations of several of the structures were conducted under hydrostatic, uniaxial, and shear loading paths. For the MD simulations, the computational cell size was increased to a $4 \times 4 \times 4$ supercell (960 atoms) in order to minimize size effects. This is particularly important since large simulation cells are required to properly accommodate large stresses and strains. For each simulation, the atomic coordinates were integrated using the leap-frog algorithm [32] with temperature and pressure controlled using algorithms due to Berendsen [33]. For each MD trajectory, atomic forces and stresses were computed by CP2K using the PBE functional and basis set as described above. Each simulation was run for 5000 time steps (1 time step = 1 fs), resulting in a total simulation time of 5 ps for each system. In order to determine the stress–strain curves for uniaxial and shear loading, small strains were applied in the desired direction at time step $t = 0$, and all strains orthogonal to the initially applied strain were allowed to relax during the remainder of the simulation. The time averaged value of the constrained stress tensor element was used to generate the stress–strain curves.

3. Results

3.1. Structures at zero stress

The lattice parameters for each structure resulting from optimization at 0 K and MD simulation at 298 K are presented in table 3. In terms of the structure at zero load, thermal effects are minimal, with slight expansion in the vector lengths and minor variations in the vector angles, resulting from inclusion of temperature effects. The distortion of the structure from purely rhombohedral symmetry is clearly evident in many of the systems and within each carbon concentration, the a lattice vector shows a larger contraction when the carbon atom resides in the polar site. It is noteworthy that many of the low carbon content stoichiometries produced structures that were either unstable elastically (negative eigenvalue in the elastic constant tensor) or converged to a minimum energy structure with a non-linear 3-atom chain. This seems to contradict some of the findings reported in earlier papers [18], however it is not clear from those publications if symmetry was enforced in their calculations in order to maintain linearity of the 3-atom chain. The bending of the 3-atom chain for these configurations was verified using a plane wave basis as implemented in the solid state DFT software package VASP [34] in place of the mixed Gaussian/plane wave basis approach in CP2K. Further, the bending of the 3-atom chain occurred in both the $2 \times 2 \times 2$ and $4 \times 4 \times 4$ supercells (indicating that the bending is not an artifact of the size of the computational cell used in this work) and was also found to occur when using the local density approximation in place of the PBE functional. It is known experimentally that at an approximately 8% carbon content, boron begins to precipitate from the lattice yielding mixtures of boron carbide and pure boron [35]. The instability of the linear 3-atom chain structure for the many of the boron-rich compositions found in this work supports this finding.

In the double zeta basis set used in this work, the polar icosahedral position is energetically favored over the equatorial site with the polar configurations being 33.9, 53.0, and 35.7 meV/atom lower in energy than their equatorial counterparts for the $B_{11}C$(CCC), $B_{11}C$(CCB), and $B_{11}C$(CBC) structures respectively when using the 0 K optimized configurations. For the $B_{13}C_2$ polytypoids, both containing 13.33% carbon, the CBC arrangement is clearly favorable over the CCB arrangement, which is 163 meV/atom higher in energy.

3.2. Elastic constants

The zero stress elastic constants (with respect to rhombohedral axes), bulk modulus, shear modulus, and Young's

Table 4. Computed zero pressure elastic moduli. All values in GPa. The three values for Young's modulus correspond to the values along the *x*, *y*, and *z* stress axes where the *z*-axis is coincident with the rhombohedrally oriented [111] direction.

Structure	Formula	% C	C_{11}	C_{12}	C_{13}	C_{14}	C_{33}	C_{44}	Bulk[a]	Shear	Young's
Experiment[37]	$B_{5.6}C$	**15.2**	**542.8**	**130.6**	**63.5**	—	**534.5**	**164.8**	**236.8**	**195.6**	**460.1**
$B_{11}C_e$(CCC)	$B_{2.75}C$	26.66	501.7	120.0	65.8	26.7	547.7	190.7	235.4	195.4	467/513/528
$B_{11}C_p$(CCC)	$B_{2.75}C$	26.66	517.9	133.1	58.7	49.1	544.4	173.4	237.4	189.9	464/498/531
B_{12}(CCC)	B_4C	20.00	486.9	188.8	64.9	14.7	518.1	133.6	221.1	173.2	451/451/504
$B_{11}C_e$(CCB)	B_4C	20.00	457.8	119.8	61.5	36.3	536.1	111.6	221.8	162.4	409/438/520
$B_{11}C_p$(CCB)	B_4C	20.00	470.3	124.6	53.6	44.6	505.7	132.5	217.8	170.9	417/441/492
$B_{11}C_e$(CBC)	B_4C	20.00	518.3	116.8	65.9	30.6	522.5	159.6	234.1	196.5	481/522/507
$B_{11}C_p$(CBC)	B_4C	20.00	534.2	120.2	58.1	38.0	525.7	168.4	233.6	199.7	494/519/514
B_{12}(CCB)	$B_{6.5}C$	13.33	395.7	139.4	82.8	61.7	393.7	96.6	202.3	135.6	291/381/373
B_{12}(CBC)	$B_{6.5}C$	13.33	531.3	105.3	54.2	−7.95	528.5	167.1	224.4	201.4	506/506/519

[a] Computed using Voigt–Reuss–Hill average.

modulus for each structure are presented in table 4. In determining the elastic constants, the minimum energy structures found using 0 K optimization (see table 3) were used and temperature effects were not included. This was done to ensure that optimized structures with maximal symmetry were used in computation of the elastic constant tensor in order to allow application of the Born stability criterion [36] for the $\bar{3}m$ point group (discussed below) to identify structural instability under load. Inclusion of temperature, in the context of MD, introduces asymmetry via the random velocities used to initiate the MD trajectories. It should be noted that only the B_{12}(CCC) and B_{12}(CBC) structures strictly adhere to $R\bar{3}m$ symmetry and the small distortions present in the other structures introduce additional non-zero, albeit small, elements in the elastic constant tensor. As a result, for ease of comparison across the range of structures, only the six non-zero C_{ij}'s that are present for $R\bar{3}m$ symmetry are presented. The elastic constants are similar in magnitude for all structures, however B_{12}(CCB) shows a considerable reduction in stiffness compared to the other systems. The experimental values in table 4 were measured by McClellan *et al* using a sample with stoichiometry $B_{5.6}C$ (15.2% C) [37]. However, in their work, the value of the C_{14} modulus was indeterminate due to the hexagonal symmetry assumed in determination of the elastic moduli. The theoretical C_{14} moduli are comparatively small and that for the B_{12}(CBC) structure is negative compared to the positive values obtained for the rest of the structures. The negative C_{14} value for B_{12}(CBC) is consistent with the result reported by Shirai [38]. The relationship of the values reported here to the so-called global minimum Young's modulus reported by McClellan *et al* [37] is not clear. In addition, past research on the boron-rich compositions has been inconclusive on the nature of $B_{13}C_2$. Early work by Samsonov [11] suggested that it was a separate phase however this is still an open question in our opinion.

The evolution of the elastic constants under hydrostatic and uniaxial load for a $B_{11}C_4$ polytypoid, two B_4C polytypes, and a $B_{13}C_2$ polytypoid are shown in figures 4–11. For the uniaxial study, compression was applied along an axis coincident with the 3-atom chain ([111] direction), which is the stiffest elastic direction in the structure. All of the elastic constants, which include the stress corrections given in

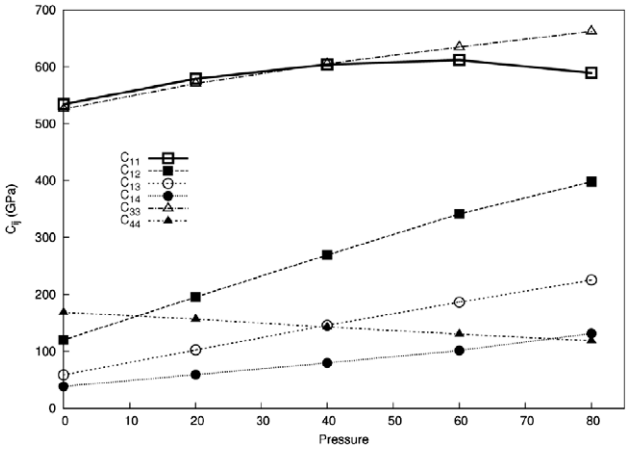

Figure 4. Stress dependent elastic constants for $B_{11}C_p$(CCC) (26% C) under hydrostatic load.

equation (2), become gradually stiffer with pressure; however, the C_{44} modulus *decreases* with load in all cases except that for uniaxial compression of the extremely carbon rich $B_{11}C_p$(CCC) (figure 8) where it remains essentially constant. This softening of C_{44} has been observed experimentally [39] and theoretically [40] in alpha quartz, which is known to undergo pressure-induced amorphization similar to that observed in BC. This softening of the C_{44} shear modulus with load may play a role in the sudden drop in shear strength of shock loaded boron carbide [21, 22].

3.3. Born stability analysis

We have applied the Born stability criterion to identify stresses at which stoichiometries within the BC structure may show an elastic instability. Born showed that an expansion of the internal energy of a crystal in a power series in the strain, along with the imposition of positivity of the energy, leads to restrictions on the relative magnitudes of the elastic constants of a stable crystal [36, 41]. Each of the elastic constants varies independently with stress, and at some critical load, the system may reach a structural instability. BC is highly anisotropic elastically, belonging to the crystallographic space group $R\bar{3}m$ with 6 independent elastic constants $\{C_{ij}\}$ and imposition of the Born stability criterion leads to the following

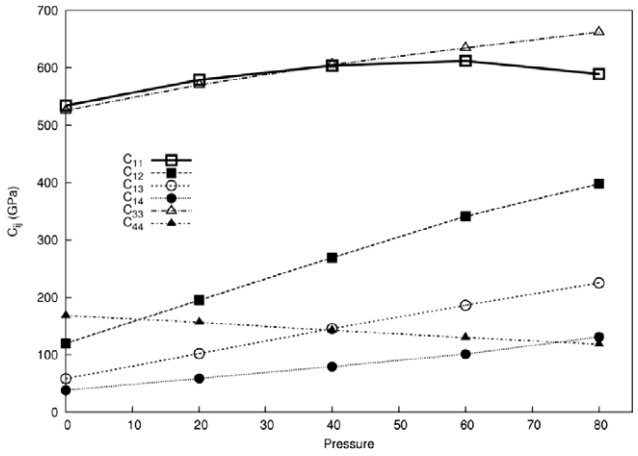

Figure 5. Stress dependent elastic constants for $B_{11}C_p$(CBC) (20% C) under hydrostatic load.

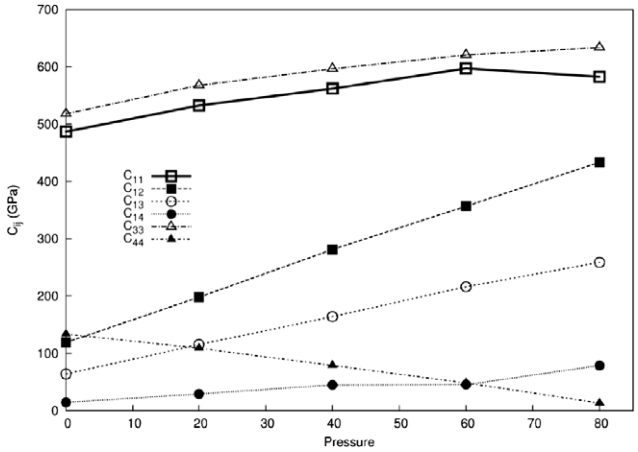

Figure 6. Stress dependent elastic constants for B_{12}(CCC) (20% C) under hydrostatic load.

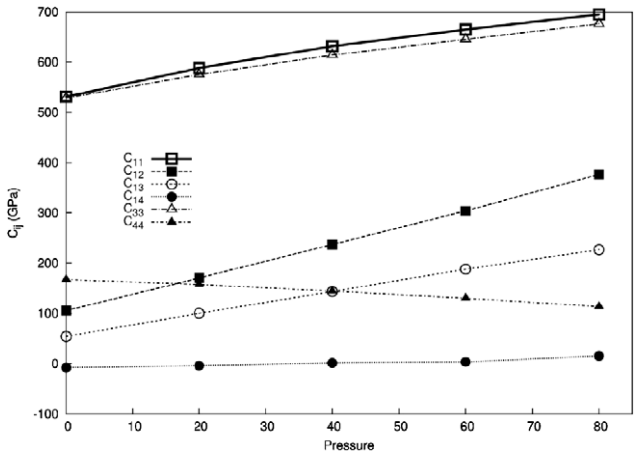

Figure 7. Stress dependent elastic constants for B_{12}(CBC) (13% C) under hydrostatic load.

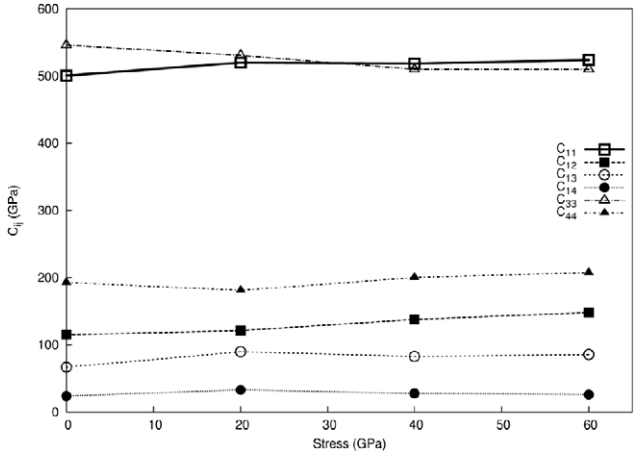

Figure 8. Stress dependent elastic constants for $B_{11}C_p$(CCC) (26% C) under uniaxial load.

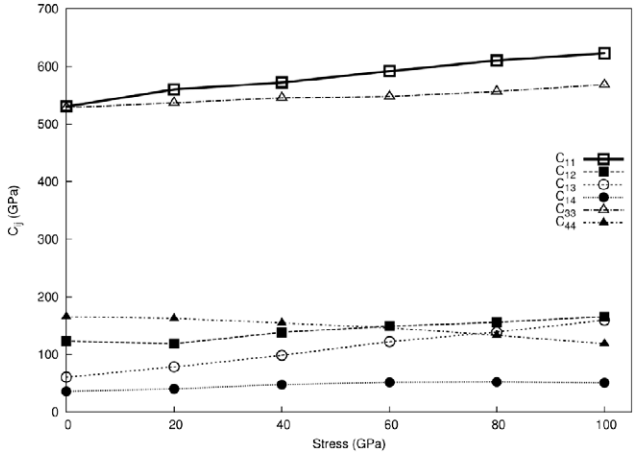

Figure 9. Stress dependent elastic constants for $B_{11}C_p$(CBC) (20% C) under uniaxial load.

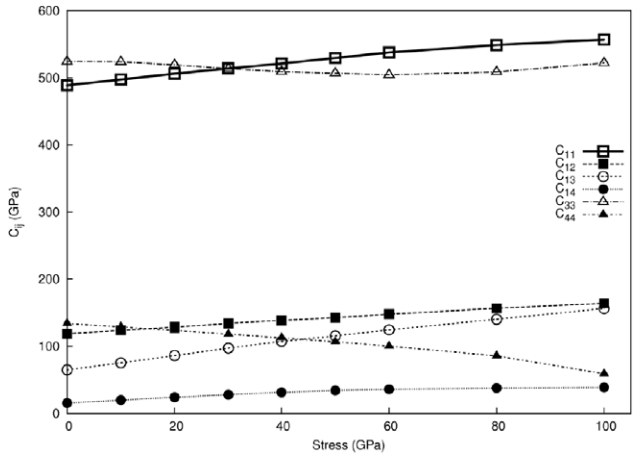

Figure 10. Stress dependent elastic constants for B_{12}(CCC) (20% C) under uniaxial load.

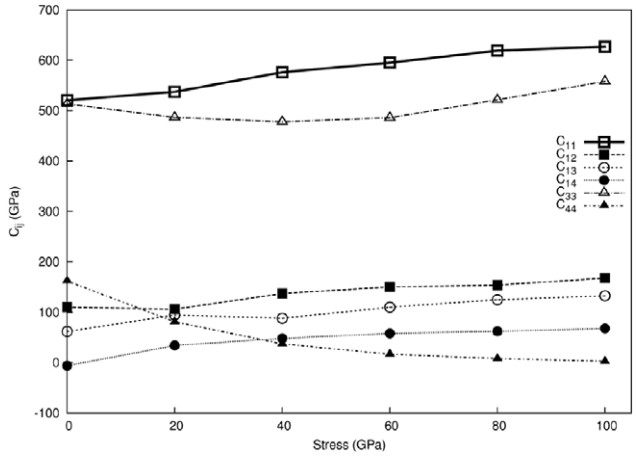

Figure 11. Stress dependent elastic constants for B_{12}(CBC) (13% C) under uniaxial load.

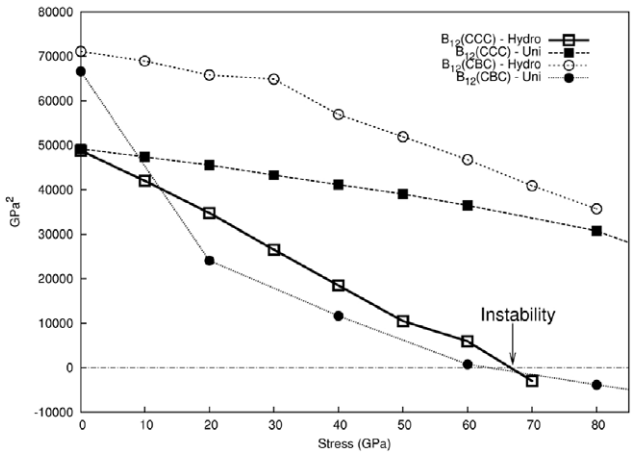

Figure 12. Born stability condition (see equation (5)) for B_{12}(CCC) and B_{12}(CBC).

restrictions on the elastic constants for the BC structure (under hydrostatic load):

$$B_{11} - |B_{12}| > 0 \tag{3}$$

$$(B_{11} + B_{12})B_{33} - 2B_{13} * B_{13} > 0 \tag{4}$$

$$(B_{11} - B_{12})B_{44} - 2B_{14} * B_{14} > 0 \tag{5}$$

where we have used the stress corrected coefficients **B** obtained from equation (2) for elastic moduli at non-zero load, as explained in [31]. The general procedure is to compute the 6 elastic constants as a function of load with evaluation of equations (3)–(5) at each point to determine the onset of the instability. Once the initial instability has been located, evaluation of the 'soft modes' of deformation (atomic displacements corresponding to the instability) can also be determined.

For most of the structures (see table 3) there is a monoclinic distortion at zero load, consistent with conclusions reached by Huhn and Widom [10]. However, for B_{12}(CCC) and B_{12}(CBC), there is no reduction in symmetry and the stability criteria presented above are strictly applicable in these cases. In both cases, the first two relations defined in equations (3) and (4) remained positive over the applied hydrostatic and uniaxial compression ranges, however the condition given in equation (5), as shown in figure 12, reaches a zero value at ≈67 GPa for the B_{12}(CCC) polytype after *hydrostatic* compression and ≈62 GPa for B_{12}(CBC) when compressed *uniaxially* along the 3-atom chain. Equation (5) is violated before the others due to the decreasing magnitude of the C_{44} elastic constant in each structure as the load is increased. Interestingly, B_{12}(CBC), which shows an elastic instability under uniaxial load, does not show a critical point over the applied range under hydrostatic load. However, the hydrostatic curve for this structure, as shown in figure 12, is trending toward zero and extrapolation of the curve suggests an instability will be reached at ≈160 GPa. Similarly, for the B_{12}(CCC) uniaxial curve, extrapolation suggests an elastic instability will occur at ≈141 GPa. The variation in mechanical response to each particular loading pattern is exemplary of the changes that can be induced by variation in the local bonding within the crystal.

Although B_{12}(CCC) and B_{12}(CBC) show an elastic instability as the stress is increased, continual loading along the same path, beyond the instability point, results in no discernible collapse of the structure. Specifically, the structure of the unit cell, for stresses beyond the instability, contains linear 3-atom chains and symmetric icosahedra although the Born criterion indicates that there is a lower energy configuration accessible beyond the critical stress under hydrostatic or uniaxial load. This suggests, at least qualitatively, that other pathways, possibly involving shear, are necessary in order to access these lower energy, lower symmetry, configurations. In the current and previous work [24, 42] the computed stresses accommodated by boron carbide without structural failure have been much higher than those suggested experimentally, however, as suggested previously [24], the conditions of the experiments may be drastically different from the idealized models used computationally. Large shear stresses, which can significantly lower phase transformation pressures [43] may be present experimentally and result in much lower critical stresses than those observed computationally along purely hydrostatic or uniaxial paths. The effect of shear on the mechanical properties of BC will be discussed below.

3.4. Equations of state

The hydrostatic compression data for $B_{11}C_p$(CCC), B_{12}(CCC), $B_{11}C_p$(CBC), and B_{12}(CBC) resulting from quantum MD simulations at 298 K, are shown in figure 13. The pressure response in the absence of shear is essentially equivalent for each structure. The resulting pressure–volume data was fitted to the third order Birch–Murnaghan equation of state [44] and the bulk modulus and pressure derivative for each structure are presented in table 5.

Experimentally, there is a reduction in the bulk modulus as the carbon concentration decreases (see table 1) and this trend is also observed in the computed bulk moduli.

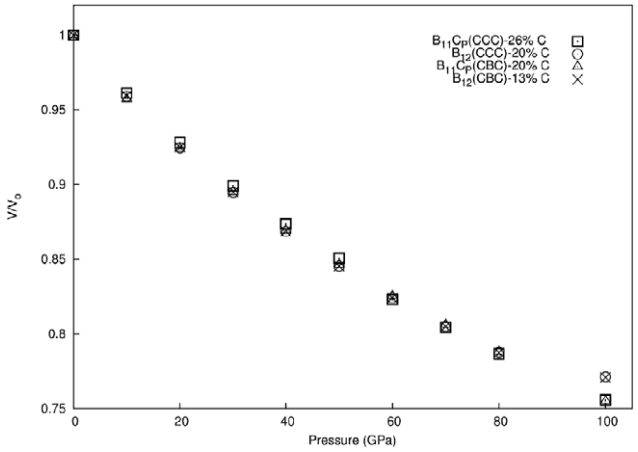

Figure 13. Pressure–volume curves for structures within each stoichiometry.

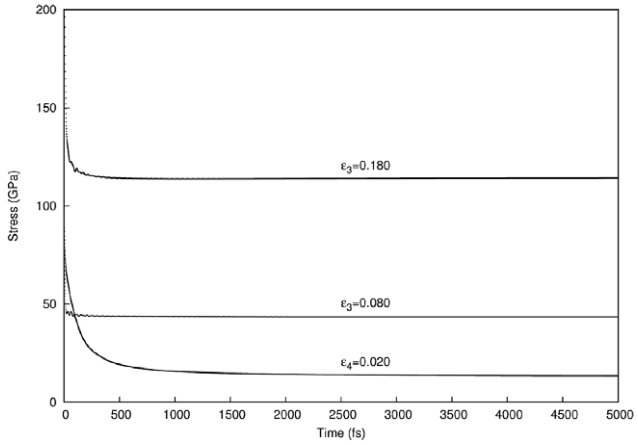

Figure 14. Time trace of the non-zero stress tensor element for simulations of B_{12}(CCC) with uniaxial compressions $\varepsilon_3 = 0.08$, 0.180 and shear strain $\varepsilon_4 = 0.02$.

Table 5. Birch–Murnaghan equation of state for structures within each carbon content.

Structure	Formula	% C	Bulk modulus (GPa)	Pressure derivative
$B_{11}C$(CCC)	$B_{2.75}C$	26.66	245.5	1.7
B_{12}(CCC)	B_4C	20.0	225.5	3.3
$B_{11}C_p$(CBC)	B_4C	20.0	226.7	3.9
B_{12}(CBC)	$B_{6.5}C$	13.3	223.9	2.7

3.5. Stress–strain curves

Stress–strain curves for each structure were computed using MD simulations at 298 K. A primary concern in analysis of the simulation results is the relatively short simulation time of 5 ps (5000 time steps) used to integrate the trajectories. Representative time traces of the constrained stress tensor element, for uniaxial and shear strain, in B_{12}(CCC) are shown in figure 14. The constrained tensor element (all others are elements are relaxed to zero stress) has reached an equilibrium value in all cases in less than 1000 time steps and remains constant for the remainder of the simulation. Therefore the simulation time of 5 ps is sufficiently long to provide converged stress–strain curves for the systems treated in this work.

Stress–strain curves for uniaxial compression along the 3-atom chain axis for $B_{11}C_e$(CCC), $B_{11}C_p$(CCC), three B_4C polytypes, and B_{12}(CBC) are shown in figure 15. The maximum stress obtained is ≈140 GPa in $B_{11}C_p$(CBC), followed by B_{12}(CBC). The carbon-rich stoichiometries with 26% carbon have curves that closely follow the others in the elastic region, however they reach a failure stress at much lower loads, ≈40 GPa, which is about 3.5 times less than that of some of the other structures. Although such carbon-rich compositions are not relevant according to the phase diagram, this still represents a dramatic demonstration of the effect of atomic structure and stoichiometry on the mechanical properties. For each material, the 3-atom chain remains linear up to the maximum stress and then an abrupt bending of the chain occurs resulting in a loss of strength. Snapshots

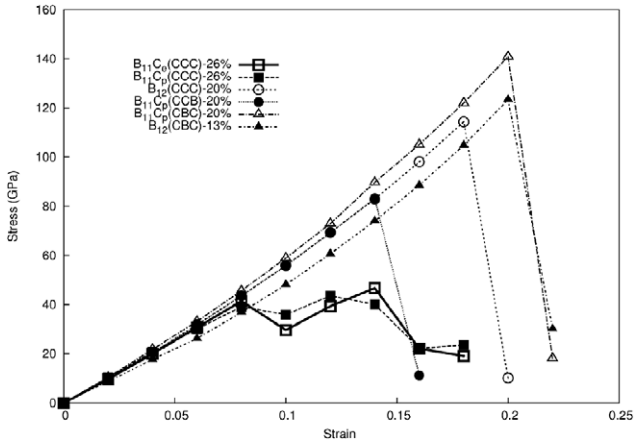

Figure 15. Stress–strain curves for uniaxial compression along axis of 3-atom chain.

of configurations, extracted from the MD trajectory for the $B_{11}C_p$(CCC) structure before and at the critical stress are shown in figure 16. The bending of the 3-atom chain at the failure point is clearly evident in the structure.

In addition to uniaxial compression, we have also simulated the strength of the structures under shear loading. Experimentally, shear loading has been identified as a critical mechanism resulting in amorphization of boron carbide [20] and the shear strength of boron carbide has been shown to be significantly reduced at stresses above the Hugoniot elastic limit [21, 22]. Stress–strain curves under shear, for several structures, are shown in figures 17–19. For each system, an ε_4 shear strain was applied incrementally, until failure, and this was done using initial configurations with uniaxial compression, σ_3, of 0, 10, 20 and 30 GPa along the 3-atom chain axis. In this way, the shear strength of the material can be simulated as a function of the uniaxial load on the system. For each material, the shear strength is substantially less than the uniaxial compressive strength and as the uniaxial load is increased there is a reduction in the shear strength, consistent with experimental observation. The reduction in shear strength is not as marked as what is seen in shock

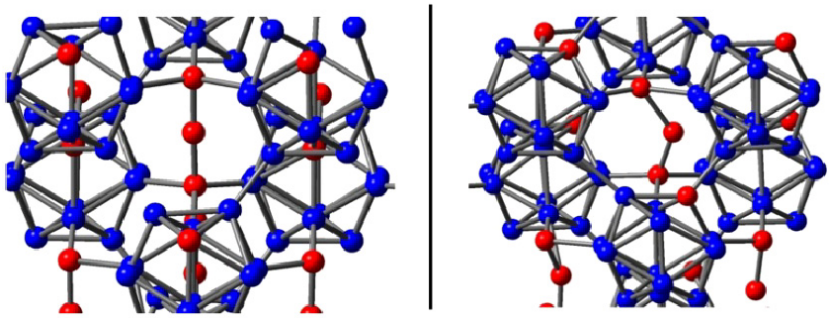

Figure 16. Snapshots of molecular dynamics simulation of $B_{11}C_p$(CCC) under uniaxial compression at 20 GPa (left) and at the failure stress, 40 GPa. Failure is associated with bending of the 3-atom chain (boron = blue, carbon = red).

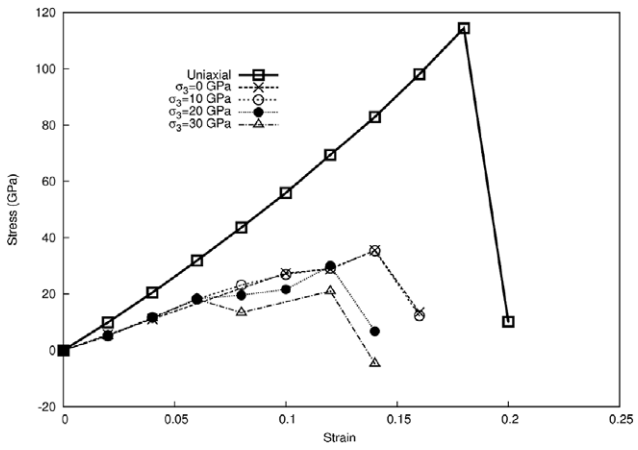

Figure 17. B_{12}(CCC) stress–strain curves resulting from shear strain, ε_4, at several values of uniaxial stress, σ_3, along the 3-atom chain axis. The uniaxial curve (also presented in figure 15), in the absence of shear, is included for reference.

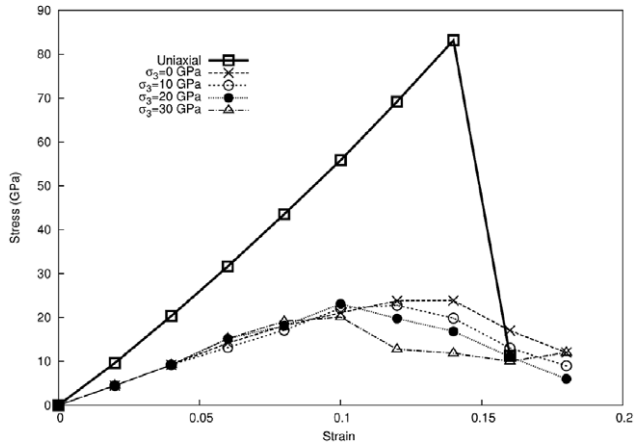

Figure 18. $B_{11}C_p$(CCB) stress–strain curves resulting from shear strain, ε_4, at several values of uniaxial stress, σ_3, along the 3-atom chain axis. The uniaxial curve (also presented in figure 15), in the absence of shear, is included for reference.

experiments. Shock loading is a much more rapid process than the essentially static loading simulations done here, however the reduction in shear strength trend is still evident in the simulated data.

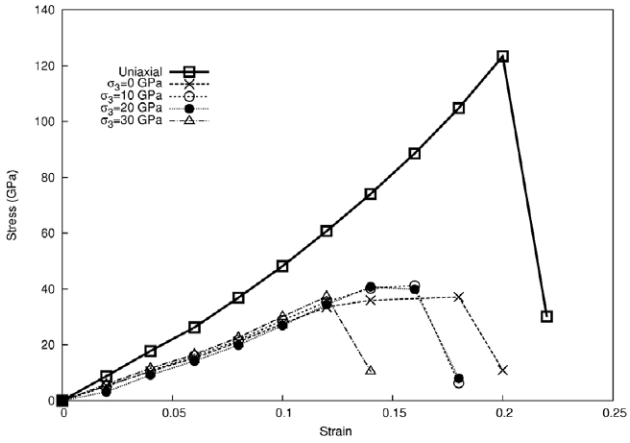

Figure 19. B_{12}(CBC) stress–strain curves resulting from shear strain, ε_4, at several values of uniaxial stress, σ_3, along the 3-atom chain axis. The uniaxial curve (also presented in figure 15), in the absence of shear, is included for reference.

In the work of Yan *et al* [25] the effect of nonhydrostatic stress on the elastic stability of BC at high pressures was examined experimentally. In that work, there was no evidence of amorphization as the pressure was increased. However, as the pressure was gradually decreased, evidence of an amorphous phase was observed, occurring at a pressure ≈20 GPa. As shown in the shear strain curves presented in figures 17 and 18, the yield strength under shear load for each structure is ≈20 GPa. Although a correlation between the experiment and the computed value can be inferred, the implication of this finding is currently not clear and will be the subject of future work.

4. Discussion and conclusion

In conclusion, atomic structure and stoichiometry have a marked effect on the calculated mechanical response of boron carbide. As shown in table 3, placement of even a single carbon atom within an icosahedron results in a monoclinic distortion of the structure which reduces the crystal symmetry via contraction of the *a* cell vector and elongation of the other cell axes. The B_{12}(CCB) structure shows a considerable reduction in stiffness, as evidenced by its C_{11}, C_{33}, and C_{44} elastic moduli, that are considerably

smaller than those of the other structures and the C_{14} modulus of the B_{12}(CBC) structure is *negative* (unlike the remaining structures) with a value of −7.95 GPa. For all structures, regardless of stoichiometry, the C_{44} elastic constant displays a negative slope in response to hydrostatic load and as a result of this C_{44} pressure softening, an elastic instability exists at values of 67 GPa and 62 GPa for the B_{12}(CCC) and B_{12}(CBC) structures respectively. The maximum yield strength under uniaxial compression is ≈140 GPa, obtained for the $B_{11}C_p$(CBC) structure (20% C), followed by the B_{12}(CBC) structure (13% C) that accommodated uniaxial loads up to ≈120 GPa before failure. Within all structures, the collapse of the unit cell is associated with an abrupt bending of the 3-atom chain axis (see figure 16). Also notable is that all of the materials, regardless of stoichiometry, exhibit pressure softening of the C_{44} modulus, in contrast to all the other moduli that increase with pressure. The consistent softening of the C_{44} modulus, regardless of stoichiometry, indicates that this is a feature of the icosahedral/3-atom chain structural framework of the BC atomic structure which is common among all of the materials. The softening of the shear moduli, and the inclusion of shear strain which lowers the yield stress considerably, suggests possible atomic structure mechanisms for the experimentally observed reduction in shear strength during shock loading experiments and the formation of nano-structured amorphous regions observed in ballistic impact experiments at pressures of about 20–25 GPa. In addition, as seen in figures 17–19, the yield strength of B_{12}(CBC) under a shear strain (30–40 GPa) is about twice that of the other structures (10–20 GPa) suggesting that it may be the most stable under shear loading. The softening of the shear moduli is associated with the formation of new bonds between the unsaturated central atom in the 3-atom chain with equatorial atoms in neighboring icosahedra. Uniaxial and hydrostatic loading decreases the spacing between the central chain and equatorial atoms and the formation of these new bonds results in an energetically more favorable configuration. Elastic constants are related to the change in configuration energy as a function of displacement and the reduction in the C_{44} modulus is driven by the formation of these new bonds between the chain and icosahedra.

Computational results have suggested structural stability under much higher loads than what is observed experimentally. It has been suggested [24] that complex strain patterns, principally involving shear, are necessary to access the lower energy, lower symmetry, configurations. Exploration of these complex shear loading paths is possible using quantum mechanical potentials, as done in this work, however the exploration of the six dimensional strain space using different combinations of strain is computationally prohibitive. This calls for the development of a classical potential applicable to icosahedral boron carbide. The Reax [45] forcefield may serve as a good functional form as it can accommodate the charge variation that occurs as a function of geometry and, through the use of bond orders, can properly model carbon atoms which exist in different hybridization states depending on their presence in chains or icosahedra. The large amount of data generated for the structures and elastic properties contained in this work can serve as a parameterization set for the development of such a classical model. Using a classical model, much larger simulations of boron carbide can be performed and studies of the structural response of boron carbide under shock loading can be performed and correlated with the available experimental shock loading data.

Acknowledgments

Financial support of this work was granted as a part of the Director's Research Initiative program at the Army Research Laboratory. All calculations were conducted using computational resources maintained by the Department of Defense High Performance Computing and Modernization Program (Challenge Project No. ARLAPC5L). The authors would also like thank Dr K T Ramesh of the Johns Hopkins University (Baltimore, MD) for many useful discussions.

References

[1] Telle R 1994 *Structure and Properties of Ceramics* ed M V Swain (New York: Wiley)
[2] Clark H K and Hoard J L 1943 *J. Am. Ceram. Soc.* **65** 2115
[3] Lazzari R, Vast N, Besson J M, Baroni S and Dal Corso A 1999 *Phys. Rev. Lett.* **83** 3230
[4] Wilson W S and Guichelaar P J 1997 *Carbide, Nitride, and Boride Materials Synthesis and Processing* ed A W Weimer (London: Chapman and Hall)
[5] Khanra A K 2007 *Bull. Mater. Sci.* **30** 93
[6] Beauvy M 1983 *J. Less-Common Met.* **90** 169
[7] Lipp A 1965 *TR Elektroschmelzwerk Kempten* reprinted from *Technische Rundschau* nos. 14, 28 and 33
Lipp A 1966 *TR Elektroschmelzwerk Kempten* reprinted from *Technische Rundschau* no. 7
[8] Domnich V, Reynaud S, Haber R A and Chhowalla M 2011 *J. Am. Ceram. Soc.* **94** 3605 and references therein
[9] Widom M and Huhn W P 2012 *Solid State Sci.* submitted
[10] Huhn W P and Widom M 2012 *J. Stat. Phys.* submitted
[11] Samsonov G V, Zhuravlev N N and Amnuel I G 1956 *Fiz. Met. Metalloved.* **3** 309
[12] McCuiston R, LaSalvia J, McCauley J and Mayo W 2009 *Proceedings of the 32nd International Conference and Exposition on Advanced Ceramics and Composites* p 153
[13] Chen M W, McCauley J W, LaSalvia J C and Hemker K J 2005 *J. Am. Ceram. Soc.* **88** 1935
[14] Conde O, Silvestre A J and Oliveira J C 2000 *Surf. Coat. Technol.* **125** 1
[15] Konovalikhin S V and Ponomarev V I 2009 *Russ. J. Inorg. Chem.* **54** 197
[16] Kwei G H and Morosin B 1996 *J. Phys. Chem.* **100** 8031
[17] Kohn W and Sham L J 1965 *Phys. Rev.* **140** 1133
[18] Saal J E, Shang S and Liu Z 2007 *Appl. Phys. Lett.* **91** 231915
[19] Vast N, Sjakste J and Betranhandy E 2009 *J. Phys.: Conf. Ser.* **176** 012002
[20] Chen M, McCauley J W and Hemker K J 2003 *Science* **299** 1563
[21] Vogler T J, Reinhart W and Chhabildas L C 2004 *J. Appl. Phys.* **95** 4173
[22] Dandekar D P 2001 *Army Research Laboratory Technical Report* ARL-TR-2456
[23] Taylor D E, Wright T W and McCauley J W 2011 *Army Research Laboratory Memorandum Report* ARL-MR-0770
[24] Aryal S, Rulis R and Ching W Y 2011 *Phys. Rev.* B **84** 184112
[25] Yan X Q, Zhang T L, Guo J J, Jin C Q, Zhang Y, Goto T, McCauley J W and Chen M W 2009 *Phys. Rev. Lett.* **102** 075505
[26] Liu D C and Nocedal J 1989 *Math. Program.* **45** 503
[27] CP2K is freely available from: http://cp2k.berlios.de/

[28] Perdew J P, Burke K and Ernzerhof M 1996 *Phys. Rev. Lett.* **77** 3865
[29] Doll K 2009 *Mol. Phys.* **108** 223
[30] Wang J and Yip S 1993 *Phys. Rev. Lett.* **71** 4182
[31] Kimizuka H, Ogata S, Li J and Shibutani Y 2007 *Phys. Rev.* B **75** 054109
[32] Allen M P and Tildesley D J 1989 *Computer Simulation of Liquid* (Oxford: Clarendon)
[33] Berendsen H J C, Postma J P M, van Gunsteren W F, DiNola A and Haak J R 1984 *J. Chem. Phys.* **81** 3684
[34] Kresse G and Furthmuller J 1996 *Comput. Mater. Sci.* **6** 15
[35] Bouchacourt M and Thevenot F 1981 *J. Less-Common Met.* **82** 219
[36] Born M and Huang K 1954 *Dynamical Theory of Crystal Lattices* (Oxford: Oxford University Press)
[37] McClellan K J, Chu F, Roper J M and Shindo I 2001 *J. Mater. Sci.* **36** 3403
[38] Shirai K 1997 *Phys. Rev.* B **55** 12235
[39] Gregoryanz E, Hemley R J, Mao H and Gillet P 2000 *Phys. Rev. Lett.* **84** 3117
[40] Binggeli N and Chelikowsky J R 1992 *Phys. Rev. Lett.* **69** 2220
[41] Grimvall G, Magyari-Köpe B, Vidvuds O and Persson K 2012 *Rev. Mod. Phys.* **84** 945
[42] Dekura H, Shirai K and Yanase A 2010 *J. Phys.: Conf. Ser.* **215** 012117
[43] Levitas V I and Shvedov L K 2002 *Phys. Rev.* B **65** 104
[44] Birch F 1947 *Phys. Rev.* **71** 809
[45] Chenowith K, van Duin A and Goddard W A 2008 *J. Phys. Chem.* A **112** 1040